1 Title: Polar pattern formation induced by contact following locomotion in a
2 multicellular system

3

4 Authors: Masayuki Hayakawa[1], Tetsuya Hiraiwa[2,3], Yuko Wada[1], Hidekazu
5 Kuwayama[4], Tatsuo Shibata[1] *

6

7 Affiliations
8 [1]Laboratory for Physical Biology, RIKEN Center for Biosystems Dynamics Research,
9 Kobe 650-0047, Japan
10 [2]Mechanobiology Institute, National University of Singapore, Singapore 117411,
11 Singapore.
12 [3]Universal Biology Institute, University of Tokyo, 7-3-1 Hongo Bunkyo-ku, Tokyo
13 113-0033, Japan
14 [4]Faculty of Life and Environmental Sciences, University of Tsukuba, Tennodai, 1-1-1,
15 Tsukuba, Ibaraki 305–8572, Japan

16

17 Correspondence should be addressed to T.S. (tatsuo.shibata@riken.jp)

18

19 **Abstract:**

20

21 **Biophysical mechanisms underlying collective cell migration of eukaryotic cells**
22 **have been studied extensively in recent years. One paradigm that induces cells to**
23 **correlate their motions is contact inhibition of locomotion, by which cells**
24 **migrating away from the contact site. Here, we report that tail-following behavior**
25 **at the contact site, termed contact following locomotion (CFL), can induce a non-**
26 **trivial collective behavior in migrating cells. We show the emergence of a traveling**
27 **band showing polar order in a mutant *Dictyostelium* cell that lacks chemotactic**
28 **activity. The traveling band is dynamic in the sense that it continuously assembled**
29 **at the front of the band and disassembled at the back. A mutant cell lacking cell**
30 **adhesion molecule TgrB1 did not show both the traveling band formation and**
31 **CFL. We thus conclude that CFL is the cell-cell interaction underlying the**
32 **traveling band formation. We then develop an agent-based simulation with CFL,**
33 **which shows the role of CFL in the formation of traveling band. We further show**
34 **that the polar order phase consists of subpopulations that exhibit characteristic**
35 **transversal motions with respect to the direction of band propagation. These**

36 **findings describe a novel mechanism of collective cell migration involving cell–cell**
37 **interactions capable of inducing traveling band with polar order**.

38

39

40

41 **Introduction**

42   The collective migration of eukaryotic cells plays crucial roles in processes such as
43 wound healing, tumor progression, and morphogenesis, and has been the focus of
44 extensive study(Haeger et al., 2015). The collective effects are typically associated with
45 cell–cell interactions, such as long-range interaction mediated by secreted chemicals or
46 short-range stable cohesive interaction mediated by adhesion molecules. However, the
47 study of self-propelled particles has revealed that motile elements which lack such
48 activities may nonetheless give rise to dynamic collective motion, such as a traveling
49 band(Chaté et al., 2008; Ginelli et al., 2010; Ohta and Yamanaka, 2014; Solon et al.,
50 2015), mediated by a relatively simple transient short-range interaction, such as
51 alignment interaction(Marchetti et al., 2013; Vicsek et al., 1995; Vicsek and Zafeiris,
52 2012). The emergence of such collective motions of self-propelled particles has been
53 observed in a wide variety of systems, ranging from animal flocks(Ballerini et al., 2008),
54 bacteria swarms(Wioland et al., 2013; Zhang et al., 2010), and cell assemblies(Szabó et
55 al., 2006) to biopolymers and molecular motors(Butt et al., 2010; Sumino et al., 2012;
56 Weber and Semmrich, 2010). For some of these systems, the connection between a
57 macroscopic collective behavior and the microscopic dynamics of its constituents has
58 been established. For instance, in biopolymers and molecular motors, traveling band
59 formation is induced by local physical interactions among constituent elements(Sumino
60 et al., 2012; Suzuki et al., 2015; Weber and Semmrich, 2010). In the case of eukaryotic
61 cells, however, there has been no report to link traveling band formation to short-range
62 cell–cell interactions.

63   The social amoeba *Dictyostelium discoideum* is a model organism for the study of
64 collective cell migration. The coordinated movement of cell population is achieved by
65 individual chemotactic motion to the cAMP gradient, which is formed in a self-
66 organized way. However, a mutant cell that lacks chemotactic activity to cAMP still
67 exhibits an organized coordinated motion that is probably mediated by cell-cell
68 contacts(Kuwayama, 2013). Here, we demonstrate that this coordinated motion is a
69 spontaneous polar order formation which phase-separates with a disordered background.
70 We further show that this polar order formation is attributable to the tail-following
71 behavior among the migrating cells, which we call contact following locomotion (CFL).

72 We find that the polar ordered phase caused by CFL has an internal structure. An agent-
73 based model with CFL further reveals that this internal structure is characteristic of the
74 CFL-induced polar order formation. Thus, we establish the link between the collective
75 behavior and the cell-cell interactions. Our findings open new possibilities that the
76 concept of self-propelled particles contributes to the understanding of a highly
77 orchestrated biological event of migrating cells in multicellular systems.

78

79 **Results**

80 **Traveling band formation of non-chemotactic *Dictyostelium* cells**

81 In the present study, we investigated collective cellular motion in a mutant strain of
82 *Dictyostelium discoideum*, known as "KI cell," which lacks all chemotactic
83 activity(Kuwayama, 2013; Kuwayama et al., 1993), and thus does not form a cell
84 aggregate under starvation conditions. Wildtype *Dictyostelium discoideum* forms an
85 aggregate as a result of chemotaxis mediated by a self-secreted extracellular
86 chemoattractant. Under starvation conditions, KI cells spread on a non-nutrient agar
87 plate show a segregation of cell density, which propagates as bands in around six
88 hours(Kuwayama, 2013), when the cell density is within a particular range ($1.0 \times$
89 $10^5 \, \text{cells} \, \text{cm}^{-2}$ to $4.0 \times 10^5 \, \text{cells} \, \text{cm}^{-2}$) (Supplementary Movie 1). Initially, the
90 traveling bands propagate in random directions with high orientational persistence.
91 When two bands collide, they appear to pass through each other, retaining their shapes
92 (Fig. 1a left) (Kuwayama, 2013). However, over time, the propagation directions
93 gradually become aligned, probably due to weak reorientation of propagation direction
94 as an effect of collisions. Finally, the bands are arranged almost periodically in space
95 with a spatial interval of about 1 mm (Fig. 1a right, b).

96 To determine the mechanism underlying this collective cellular motion, we
97 conducted high-magnification observations. At around 16 hours after cells were seeded
98 on an agar plate, a punched-out section of the agar plate was placed upside down on the
99 glass slide, such that the monolayer of cells was sandwiched between agar and glass
100 (Fig. S1a). These cells formed a high-density area that moved as a band in low-density
101 area for long periods of time with high orientational persistence (Fig. 1c,d and
102 Supplementary Movie 2). Whereas the cells in high-density area are packed without
103 extra space, and thus the cell density is similar across different samples (Fig. S1c), the
104 size W of the band along the propagation direction showed a broad distribution, ranging
105 from $W = 200 \, \mu\text{m}$ to $700 \, \mu\text{m}$ (N=10). In contrast, the traveling speed $\langle v_b \rangle = 0.5 \pm$
106 $0.03 \, \mu\text{m/s}$ (N=10) was consistent among different bands, independent of size W (Fig.
107 S1b).

108

Analysis of single cell trajectories

110   To study the relationship between these collective behaviors and the migration of
111 individual cells, we next performed cell-tracking analysis. Cellular movements were
112 recorded by tracing the motion of fluorescent microbeads that were incorporated into
113 the cells by phagocytosis. Figure 2a shows typical trajectories of individual KI cells.
114 The distribution of migration speeds indicates that cell migration speed inside the band
115 is slightly faster than that outside the band (Fig. 2b). The average migration speeds of
116 individual cells inside and outside the band were $v_{in} = 0.38 \pm 0.14$ µm s^{-1} and $v_{out} =$
117 0.30 ± 0.16 µm s^{-1}, respectively. The migration direction of the cells inside the band
118 was distributed around the direction of band propagation, while the migration direction
119 outside the band was distributed almost uniformly (Fig. 2c). The mean squared
120 displacement (MSD) inside the band was proportional to t^2 for more than 10^3 s (Fig.
121 2d). In contrast, the MSD outside the band exhibited a transition at around 100 s. from a
122 persistent motion proportional to t^2, to a random motion proportional to t , which
123 indicates that this motion can be described as a persistent random motion with no
124 preferred direction (Fig. 2d). This observed directional randomness reflects the effects
125 of cellular collisions, as well as its intrinsic nature of single cells. In sum, cells inside
126 the band exhibit directionally persistent motions, whereas cells outside move randomly.

127

Propagation of cell density profile

129   We then compared the average cell speed inside the band v_{in} and the band
130 propagation speed v_b, (Fig. 2e), and found that the band propagates faster than the cell
131 migration speed for all samples investigated. This implies turnover of cells in the band,
132 and that the band is continuously assembled at the front of the band and disassembled at
133 the back. Thus, it is the cell density profile that shows propagation as a
134 band(Kuwayama, 2013).

135

Analysis of multicellular movement reveals polar order formation

137   To quantitatively characterize the multicellular movement, we introduce the local
138 polar order parameter, $\varphi(n,t) = \left| \langle \boldsymbol{v}_i(t)/|\boldsymbol{v}_i(t)| \rangle_{i \in \mathcal{L}(n)} \right|$, obtained from the
139 instantaneous cell velocity $\boldsymbol{v}_i(t)$, where $\mathcal{L}(n)$ is the nth domain along the direction of
140 band propagation (see Supplementary text). In the high-density region that propagates
141 as a band, $\varphi(n,t)$ reaches around 0.8, while $\varphi(n,t)$ in the low-density area remained
142 below 0.4 (Fig. 3a). Thus, the high-density region is polar-ordered phase, which
143 propagates in the low-density disordered phase. The polar order parameter of the band

144   showed intersample variability, and was distributed from 0.6 to 0.85 (Fig. 3b). We

145   found that the order parameter of band was positively correlated with the width of band

146   *W* (Fig. 3b).

147

148   **Internal structure in the polar ordered region**

149   The polar order phase is not completely homogeneous with respect to migration

150   direction, but exhibits heterogeneity; this is related to the underlying assembly

151   mechanism. This heterogeneity can be visualized in the velocity field obtained by

152   optical flow, in which the direction of cell migration can be distinguished by color (Fig.

153   3c and Supplementary movie 3). The size-dependent squared local order parameter

154    $\langle \varphi_\ell^2(s) \rangle$ (see Supplementary text) shows a logarithmic decay with area S (Fig. 3e),

155   indicating that this heterogeneity is not spatially uncorrelated. Within the band (Fig. 3c

156   bottom), the migration direction was widely distributed from about 145 to 210 degrees

157   (a black line in Fig. 3f). The probability density functions (pdf) of the migration

158   direction obtained for the four regions (Fig. 3c bottom (i–iv)) show peaks at different

159   directions (Fig. 3f), indicating the presence of two subpopulations; one in which the

160   migration direction is ~160º (regions (ii) and (iv)) and another in which it is ~190º

161   (regions (i) and (iii)). These two subpopulations are also recognized in Fig. 3c (bottom)

162   as the regions with dark blue and light green colors, respectively, forming stripes. These

163   two types of stripes extend perpendicular to the direction of band propagation, and are

164   alternately arranged. The typical width of the stripe was around 125 μm, as determined

165   by the analysis of autocorrelation function (Fig.S2a). The kymograph in Fig. 3d shows

166   the temporal evolution of the velocity field along the line PQ in Fig. 3c, indicating that

167   the stripes (light green and dark blue) are almost immobile, suggesting that the same

168   cells experience the two stripes sequentially. From a reference frame co-moving with

169   the band, cells move from the front to the end, during which they move downward in a

170   stripe, and then move upward in another stripe (Fig.S2b). These analyses illustrate that

171   the polar order phase possesses an internal structure with respect to the migration

172   direction.

173

174   **Contact following locomotion is the cell-cell interaction that induces polar pattern**

175   **formation**

176   The formation of a polar-ordered phase with an internal structure is ultimately

177   related to the microscopic interactions between individual cells, which are short-ranged.

178   In the low-density region, cells are not completely isolated, but rather are often

179   associated with each other, migrating in single files (Fig.4a and Supplementary movie

180   4). This tail-following behavior has been described for wild-type *Dictyostelium* cells
181   within aggregation streams(Dormann and Parent, 2002). We call this behavior "contact
182   following locomotion" (CFL). In low-density assay, when two cells collide, they either
183   form CFL (Fig. 4b and Supplementary movie 5) or not (Fig. S3a). To quantitatively
184   characterize CFL, we measured the duration of cell–cell contact after two cells collide.
185   During the formation of CFL, the typical cell-to-cell distance is given by $d_a = 24$ μm.
186   We measured the time interval during which the distance is less than d_a from the time
187   series of the distance between two cells (Fig. S3b). As shown in Fig.4c, in half of the
188   cases, cell–cell contact persists for more than 300 sec. To determine whether cells that
189   form contacts for >300 sec exhibit tail-following behavior, we measured the average
190   angle a of the angles a_1 and a_2, which are the angles of the velocity vectors $\boldsymbol{v}_1$ and $\boldsymbol{v}_2$
191   with respect to the vector connecting the two cell centers $\boldsymbol{d}$, respectively (Fig. 4d). In
192   almost 60% of all cases, the angle a is 0–30º (Fig. 4e), indicating tail-following type
193   CFL.
194   To determine whether CFL is responsible for the collective behavior of KI cells, we
195   sought a mutant cell that lacks CFL activity. A knockout mutant that fails to express the
196   cell–cell adhesion molecule TgrB1 exhibits reduced CFL activity(Fujimori et al., 2019).
197   TgrB1 is known to mediate cell–cell adhesion via a heterophilic interaction with its
198   partner TgrC1(Fujimori et al., 2019; Hirose et al., 2011; 2015; C.-L. F. Li et al., 2015).
199   We first assessed whether the *tgrb1* null mutant forms propagating bands. As in the
200   control case, under starvation conditions, we spread the *tgrb1* null mutant cells on a
201   non-nutrient agar plate at a cell density of 2.0 to 3.0×10^5 cells cm^{-2} (see Methods).
202   However, neither segregation of cell density nor propagating bands appeared
203   (Supplementary movies 6 and 7.).
204   We then compared locomotive activity between control cells and *tgrb1* null mutants.
205   The velocity auto-correlation functions $C(\tau)$ of the isolated single cells showed similar
206   behaviors (Fig. S3c), indicating that locomotive activity was comparable between KI
207   cells and the *tgrb1* null mutant cells. We next quantitatively characterized the formation
208   of cell–cell contacts. We found that in 80% of all cases, cell–cell contact is disrupted
209   before 300 sec (Fig. 4f), and that only 10% of cells established CFL (Fig. S3d). In
210   particular, in half of all cases, the cell–cell distance becomes larger than d_a in 120 sec,
211   indicating that these cells failed to establish cell–cell contact. Our analyses illustrate that
212   in the *tgrb1* null mutant, CFL is nearly absent. We conclude that CFL is essential for the
213   segregation of cell density and the formation of propagating bands.
214

215 **Mathematical modeling of polar pattern formation driven by contact following**
216 **locomotion.** The collective motion of KI cells induced by the CFL interaction can be
217 modeled by an agent-based simulation(Hiraiwa, 2019). In the model, particle i at
218 position $\mathbf{r}_i$ self-propels at a constant velocity v_0 in the direction of its own polarity $\mathbf{q}_i$
219 subjected to white Gaussian noise. Thus, without interactions, the particles exhibit a
220 persistent random walk(Hiraiwa et al., 2014). The effect of CFL is introduced so that
221 polarity $\mathbf{q}_i$ orients to the location of the adjacent particle j, when particle i is located at
222 the tail of particle j (parameterized by ζ). In addition to this effect, the particles interact
223 with each other through volume exclusion interaction, adhesion, and the effect of
224 polarity $\mathbf{q}_i$ orienting toward the direction of its velocity $\mathbf{v}_i = d\mathbf{r}_i/dt$ (parameterized by
225 α). For a fixed parameter set ($\alpha = 0.4$; see Supplementary text), without CFL ($\zeta = 0$),
226 the collective behaviors did not form (Fig. S4). In contrast, with CFL ($\zeta \geq 0.1$), a polar-
227 ordered phase appeared as a propagating band in the background of disordered phase
228 (Fig. 3g and Supplementary movies 8). The speeds of the traveling band and particles
229 within the band were 0.96 and 0.9, respectively, relative to the speed of isolated
230 particles, indicating that the band is dynamic with assembly in the front and
231 disassembly in the tail, consistent with our experimental results. From the spatial pattern
232 shown in Fig. 3gh, in which the migration direction is indicated by color code,
233 heterogeneity in the migration direction is recognized within the polar-ordered phase. In
234 the simulation, we studied the pdf of migration direction in regions, whose size is
235 comparable to that in Fig. 3c ((i)–(iv)), and found that the pdf exhibited peaks at
236 different directions (Fig. 3i), similar to our experimental results (Fig. 3f). To determine
237 whether this formation of internal structure is a characteristic of propagating bands
238 induced by CFL, we studied a propagating band formed by increasing alignment effect
239 α without CFL ($\zeta = 0$), and found that the pdfs of migration direction exhibit peaks at
240 closely similar positions, indicating that the migration direction in the ordered phase is
241 more homogeneous (Fig. S5e). Thus, the formation of internal structure appears to be a
242 characteristic of the collective behavior induced by CFL. The size-dependent squared
243 local order parameter $\langle \varphi_\ell^2(s) \rangle$ (see Supplementary text) also shows the characteristic
244 decay with a logarithmic dependence on area S (Fig. 3e), as observed experimentally.

245 **Discussion**
246   In this study, we report that a mutant of *Dictyostelium* cell that lacks all chemotactic
247 activity exhibits spontaneous segregation into polar ordered solitary band. This pattern
248 formation is attributable to the cell-cell interaction called contact following locomotion
249 (CFL). The agent-based model that includes CFL reproduces the observed macroscopic

250 behaviors. Thus, we establish a link between the microscopic cell-cell interactions and
251 the macroscopic polar pattern formation.

252 We showed that the width of band is distributed widely from $W = 200$ μm to 700
253 μm (Fig. S1b). The local cell density within the band is similar across different samples
254 (Fig. S1c), suggesting that the local cell density may not be a relevant factor. In contrast,
255 we found the positive correlation between the width and the order parameter within the
256 band (Fig. 3b). We speculate that if the correlation in the migration direction is
257 gradually decorrelated from the front to the end of the band, bands with lower order
258 parameters will be more prone to larger decorrelation in the migration direction.
259 Consequently, we expect that the stronger the polar order, the wider the band width W.

260 One characteristic behavior of the present polar pattern formation is the formation of
261 internal structure, which consists of subpopulations with transversal motions. From the
262 numerical simulation result, this formation of subpopulation was not seen in the model
263 without CFL. Thus, the internal structure is a characteristic of CFL induced polar
264 pattern formation. Resolving how fluctuations in the migration direction perpendicular
265 to the band propagation direction grow to form subpopulations when CFL is present
266 remains a question for future study.

267 In this paper, we mainly focused on the behavior of single solitary band. We studied
268 the traveling band, which was well separated from other bands. Thus, all properties of
269 single solitary band studied in this paper is independent of interaction between different
270 bands. In some area, the traveling bands are arranged almost periodically in space with
271 a spatial interval of about 1 mm (Fig. 1b). How bands interact with each other to reach a
272 periodic spacing and whether the interval is independent of band width W are to be
273 investigated.

274 Wildtype *Dictyostelium discoideum* usually aggregates through chemotaxis to form a
275 hemispherical mound with a central tip region that regulates the formation of slug-like
276 multicellular structure(Williams, 2010). Whereas the KI cell alone does not show this
277 activity, KI cells are able to spontaneously migrate to the central tip region transplanted
278 from a wildtype slug and undergo normal morphogenesis and cell differentiation; this is
279 not observed in mutant KI cells lacking tgrB1(Kida et al., 2019), suggesting that tgrB1-
280 dependent CFL without chemotaxis allows KI cells to spontaneously migrate in slug.
281 Furthermore, in wildtype cells, the chemical guidance cue has been shown to cease
282 during the multicellular phase, which suggests that an alternative mechanism induces
283 collective cell migration in the multicellular body(Hashimura et al., 2019). We propose
284 that polar order formation induced by CFL plays an important role in late-stage
285 morphogenesis in this organism. Contact following locomotion, or chain migration,

286   have been reported in other cell types(D. Li and Wang, 2018). The macroscopic

287   behaviors reported in this paper may thus be found in other systems as well.

288

289

290 **Materials and Methods**

291 **Culture condition of KI mutant cells and cell density measurement.**

292 1 mL of *Klebsiella aerogenes* suspended in 5LP medium (0.5% Lactose, 0.5% bactopeptone

293 211677, Optical density = 0.1) was spread on the 9 cm 5LP plate (0.5% Lactose, 0.5%

294 bactopeptone 211677, 1.5% agar), 5LP medium dried, the non-chemotactic *Dictyostelium*

295 *discoideum*, KI mutant cells were inoculated on the plate. The KI cells were incubated for about

296 five days at 21 ºC. After cultivation, the KI cells and *Klebsiella* on the plate were collected with

297 a phosphate buffer (PB). To remove the *Klebsiella*, the suspension was centrifuged and discard

298 as much of the supernatant liquid as possible by aspiration, then clean PB was added. After

299 repeating this process two times, the number of cells was counted using a hemacytometer.

300

301 **Macroscopic observation of the traveling bands.**

302 The washed KI cells were spread (cell density = 5.0×10^5 cells/cm^2) on a 9 cm non-nutrient agar

303 plate (1.5% agar) to cause starvation. After drying of the PB, the plate was scanned every 15

304 minutes using a film scanner (V850, EPSON). The brightness in scanner images is inversely

305 correlated with cell density(Takeuchi et al., 2014). For Fig 1a and b, the original images were

306 inverted with color that depends on time points.

307

308 **Microscopic observation of the traveling bands.**

309 The KI cells were spread (cell density = 2.0 to 3.0×10^5 cells/cm^2) on the non-nutrient agar plate

310 and incubated at 21 ºC for around 16 hours. A punched piece of the agar plate was placed

311 upside down on the glass slide, and the travelling bands between the agar and glass was

312 observed by phase contrast imaging using an inverted microscope (TiE, Nikon with a 20x

313 phase-contrast objective, equipped with an EMCCD camera (iXon+, Andor)).

314

315 **Tracking analysis of individual KI cells.**

316 For the tracking analysis, 1 μL of the PB including 3% fluorescent microbeads (ex:441, em:486,

317 1.0 μm, Polysciences, Inc.) was spread at the same time with the KI cells. The trajectories of the

318 microbeads were automatically tracked by using the ParticleTracker 2D, a plugin for Image J

319 (National Institutes of Health, USA). To eliminate the trajectories of the microbeads that was

320 not internalized by the KI cells, if $|v_{cell}|$ was slower than 0.25 μm/s for 300 second continuously,

321   we excluded such trajectories. We also excluded the short trajectories of which continuous

322   tracked time was shorter than 1 hour.

323

324   **The mean squared displacement (MSD).**

325   The MSD (Fig.2d) was calculated using the formula below.

326
$$\text{MSD}(\Delta t) = \frac{1}{N(T - \Delta t)} \sum_{i=1}^{N} \sum_{t}^{T-\Delta t} \{r_i(t + \Delta t) - r_i(t)\}^2 \, ,$$

327   where Δt, T, and N means a time interval, final time, and number of the trajectory, respectively.

328

329   **Local polar order parameter.**

330   To obtain the local polar order parameter $\varphi(n, t)$ shown in Fig. 3a, the picture shown in fig 1c

331   was divided into n sections with width Δx (μm), and the order parameter was calculated in each

332   section at each time from the trajectories obtained by the tracking analysis. The local order

333   parameter φ is defined as

334
$$\varphi(n, t) = \left| \frac{1}{N(n)} \sum_{i \in \mathcal{L}(n)} \frac{v_i(t)}{|v_i(t)|} \right| ,$$

335   where $\mathcal{L}(n)$ is the set of cells that satisfy $(n - 1)\Delta x \leq x_i \leq n\Delta x$, $N(n)$ is number of the cells in

336    $\mathcal{L}(n)$, v_i and x_i are the velocity and x-position of i-th fluorescent microbeads, respectively. In this

337   study, $n = 14$ and $\Delta x = 119$ μm.

338

339   **Optical flow analysis.**

340   Optical flow analysis was performed based on the Gunnar-Farneback method using OpenCV

341   library. In the optical flow analysis, the displacement of each pixel in the original pictures are

342   characterized by coloring based on the HSV ("hue", "saturation", "value") representation. The

343   "hue" varies depending on angular variation of each pixel. In this study, a "saturation" and

344   "value" of the processed images via optical flow was fixed to 150 and 255, respectively. The

345   sequential images of the traveling band used for this analysis were taken every 2 seconds.

346

Size-dependent squared local order parameter.

To characterize the internal structures of the traveling band, the size-dependent squared local order parameter $\langle \varphi_\ell^2(S) \rangle$ is introduced (Fig.3e). To obtain the size-dependent squared local order parameter, we first calculate the squared polar order parameter $\varphi_\ell^2(S)$ within a ROI of size S, which is defined as

$$\varphi_\ell^2(S) = \frac{1}{S^2}\left\{\left(\sum_{(x,y)\in ROI} \cos\Theta(x,y)\right)^2 + \left(\sum_{(x,y)\in ROI} \sin\Theta(x,y)\right)^2\right\}$$

where $\Theta(x,y) = hue \times (360/255)$ indicates the angular variation of the pixel at position (x,y). The value of *hue* was obtained from the optical flow analysis (Fig. 3c). Then, $\varphi_\ell^2(S)$ is averaged over the entire area to obtain $\langle \varphi_\ell^2(S) \rangle$. If $\Theta(x,y)$ is a random number without spatial correlation, as the increase of the area S, $\langle \varphi_\ell^2(S) \rangle$ is expected to decay in proportion to S^{-1}.

Autocorrelation function of transverse motion with respect to the band propagation direction.

Because the band show propagation in *x*-direction, autocorrelation function of transverse motion $C_{\sin}$ is defined using *y*-component of motion as

$$C_{\sin}(\Delta x) = \frac{1}{Y(X - \Delta x)}\sum_{y=1}^{Y}\sum_{x=1}^{X-\Delta x}\sin\Theta(x,y)\sin\Theta(x + \Delta x, y),$$

where Δx is pixel interval along the *x*-axis. $C_{\sin}$ was plotted after that unit of Δx is converted to the length.

Preparation of *tgrb1* null mutant cells.

The gene disruption construct for *tgrB1* was synthesized by a polymerase chain reaction (PCR)-dependent technique (Kuwayama et al., 2002). Briefly, the 5 -flanking region of the construct was amplified with two primers, 5- CAACAGGTGGAGACTTCGGG-3 and 5-GTAATCATGGTCATAGCTGTTTCCTGCAGGCCAGCAGTAATAGTTGGAG-3. The 3-

371   flanking region of the construct was amplified with primers, 5-

372   CACTGGCCGTCGTTTTACAACGTCGACGAGAACTGTTGATTCTGATGG-3 and 5-

373   CTTGGTCCTGAACGAACTCC-3. The bsr cassette in the multicloning site of pUCBsr Bam

374   [Adachi et al., 1994] was amplified using the primer pair 5-

375   CTGCAGGAAACAGCTATGACCATGATTAC-3 and 5-

376   GTCGACGTTGTAAAACGACGGCCAGTG-3, both of which are complementary to the two

377   underlined regions, respectively. The three amplified fragments were subjected to fusion PCR

378   that produced the required gene-targeting construct. The gene-targeting constructs were cloned

379   using a TOPO TA cloning kit for sequencing (ThermoFisher Scintific MA, USA).The linear

380   construct was amplified by PCR using the outermost primers up to 10 μg. and transformed into

381   KI-5 cells. The KO clones were selected by genomic PCR using the outermost primers.

382

383   Culture condition and starvation treatment of *tgrb1* mutant null cells.

384   The *tgrb1* null cells were cultured in HL5 medium (1.43% Proteose Peptone 211684, 0.72%

385   Yeast Extract212750, 1.43% Gulcose, 0.05% KH_2PO_4, 0.13% $Na_2HPO_4 12H_2O$) at 21 degree

386   Celsius. After reaching confluent, cells on the bottom were peeled off and collected, then

387   washed two times with a centrifuge and PB. Next, the *tgrb1* null cells were transferred on the

388   1/3 SM plate (0.33% Gulcose, 0.33% bactopeptone 211677, 0.45% KH_2PO_4, 0.3% Na_2HPO_4,

389   1.5% agar) with *Klebsiella* suspension, and incubated for around two days at 21 ºC. After,

390   through the wash and count, the *tgrb1* null cells were spread on the non-nutrient agar plate, after

391   which the plate was scanned every 15 minutes using the film scanner.

392

393   Characterization of the contact following locomotion

394   The KI cells and *tgrb1* null cells for the collision assay were scraped from the traveling bands

395   and surface of the plate, respectively. The scraped cells were placed on the non-nutrient agar

396   and sandwiched with the glass. After around one hour incubation at 21 ºC, binary collisions of

397   two cells were observed by microscopy and recorded every 15 seconds. The motion of the cells

398   was tracked manually using the Manual Tracking, a plugin of Image J. Here, collision was

399   defined as the contact of pseudopods.

400

401   The velocity autocorrelation function.

402   Firstly, the migrations of the KI and *tgrb1* null mutant cells were recorded every 20 s for 60 min.

403   Here, to extract an intrinsic locomotive activity of the cells, interactions with other cells, wall,

404   and etc. were eliminated. Using obtained trajectories of cells that migrate with the velocity *v*,

405   the velocity autocorrelation function $C(\tau)$ was calculated. $C(\tau)$ is described with the form of

406
$$C(\tau) = \frac{1}{N(T-\tau)} \sum_{i=1}^{N} \sum_{t}^{T-\tau} \{\boldsymbol{v}_i(t+\tau) - \boldsymbol{v}_i(t)\}^2,$$

407   where τ, t, T, and N means a time interval, time, final time, and number of the trajectory,

408   respectively (Fig. S3c).

409

410   Modeling collective motion induced by contact following locomotion.

411   The collective motion of KI cells induced by the CFL interaction can be modeled by an agent-

412   based simulation. In the model, self-propelled particle i at position $\mathbf{r}_i$ moves at a constant

413   velocity v_0 in the direction of its own polarity $\mathbf{q}_i$ subjected to white Gaussian noise. Thus,

414   without interactions, the particles exhibit persistent random walk(Hiraiwa et al., 2014).

415   Collective motion can be modeled by assuming particle-particle interactions(Hiraiwa, 2019).

416   We firstly assume that the particles interact with each other through volume exclusion

417   (parameterized by β) and adhesion (parameterized by γ). We also assume the feature that the

418   polarity of each particle orients to the direction of its velocity $\mathbf{v}_i = d\mathbf{r}_i/dt$ (parameterized by

419   α); it is known that this assumption can effectively give rise to the alignment interaction

420   between the particles when it is combined with the volume exclusion effect(B. Li and Sun,

421   2014). (Therefore, we simply refer to this feature as alignment effect in the main text.) As the

422   main focus of this article, we incorporate CFL into this model by assuming the particle-particle

423   interaction by which polarity $\mathbf{q}_i$ orients to the location of the adjacent particle j when particle i

424   is located at the tail of particle j (parameterized by ζ). The equation of motion for the particle i

425   are then given by

426
$$\frac{d\mathbf{r}_i}{dt} = v_0 \frac{\mathbf{q}_i}{|\mathbf{q}_i|} - \beta \sum_{j \in \mathcal{N}(i)} R \frac{\mathbf{r}_j - \mathbf{r}_i}{|\mathbf{r}_j - \mathbf{r}_i|^2} + \gamma \sum_{j \in \mathcal{N}(i)} \frac{\mathbf{r}_j - \mathbf{r}_i}{|\mathbf{r}_j - \mathbf{r}_i|} \tag{1}$$

427
$$\frac{d\mathbf{q}_i}{dt} = I\mathbf{q}_i(1 - |\mathbf{q}_i|^2) + \mathbf{C}_i + \alpha \frac{\mathbf{v}_i}{|\mathbf{v}_i|} + \boldsymbol{\xi}_i \tag{2}$$

428   where the second and third terms on the right-hand side of Eq.(1) are the effects of volume

429   exclusion and adhesions, respectively. Here, $\mathcal{N}(i)$ is a set of particles that are contacting with

430   the particle i, i.e., the particle $j \in \mathcal{N}(i)$ satisfies $|\mathbf{r}_j - \mathbf{r}_i| \leq R$. On the right hand side of Eq.(2),

431   the first term shows the self-polrization, the third term gives the effect that the polarity orients

432   to the velocity direction $\mathbf{v}_i/|\mathbf{v}_i|$, the last term is white Gaussian noise with $\langle \boldsymbol{\xi}_i \rangle = (0,0)$ and

433    $\langle \boldsymbol{\xi}_i(t) \cdot \boldsymbol{\xi}_j(t') \rangle = \sigma^2 \delta_{ij} \delta(t - t')$, and the second term $\mathbf{C}_i$ describes the CFL, parameterized by ζ,

434   given by

435
$$\mathbf{C}_i = \frac{\zeta}{2} \sum_{j \in \mathcal{N}(i)} \frac{\mathbf{r}_j - \mathbf{r}_i}{|\mathbf{r}_j - \mathbf{r}_i|} \left(1 + \frac{\mathbf{q}_i}{|\mathbf{q}_i|} \cdot \frac{\mathbf{r}_j - \mathbf{r}_i}{|\mathbf{r}_j - \mathbf{r}_i|} \right). \tag{3}$$

436   Here, when the polarity of particle j, $\mathbf{q}_j$, and the vector from particles i to j, $\mathbf{r}_j - \mathbf{r}_i$, are in the

437   same orientation, the maximum following effect is exerted on particle i to the direction of

438   particle j. Such a situation is expected when particle i is located in the tail of particle j with

439   respect to the polarity $\mathbf{q}_j$. In contrast, when particle i is located in the front of particle j, $\mathbf{C}_i$

440   almost vanishes. The simulation is implemented within a square box of size L with periodic

441   boundary condition. For all simulations, we used fixed parameter values except ζ and α, given

442   by $v_0 = 1.0$, $\beta = 1.0$, $R = 1.0$, $\gamma = 1.20$, and $\sigma^2 = 0.4$. For I in Eq.(2), we consider the

443   situation where I is infinitely large, so that $\boldsymbol{q}$ was projected onto the unit vector $|\boldsymbol{q}| = 1$ for the

444   numerical simulation. The density of particles per unit area ρ is given $\rho = 1$. The number of

445   particles n is $n = 80,000$ (Fig. 3ghi and Fig. S5) and $n = 10,000$ (Fig. S4).

446

Histogram of migration direction in the numerical results.

448   Firstly, we selected only the ROIs in the vicinity of the band front in the following way: We

449   define a ROI as being within the bands if the particle density is higher than 1.16, which

450   corresponds to the 2D dense packing fraction of disks, ~0.91. Using this definition, we define

451   the ROI as being vicinity of the band front if the ROI is within the band at the last F_{ana} frames

452   whereas it is out of the band at the frames between the last $F_{ana} + F_{wait} + F_{out}$ and the last

453    $F_{ana} + F_{wait}$. In other words, F_{ana} means the number of frames to be analyzed and must be

454   within the band, F_{out} means the number of frames to determine the band front (i.e. the frames in

455   which the ROI must be still out of the band assuming that the band travels only in one direction),

456   and F_{wait} means the number of the waiting frames (i.e. the frames which are not used at all)

457   between these frame sets.

458   The results of this algorithm for CFL-induced ($\zeta = 0.1, \alpha = 0.4$) and alignment-induced ($\zeta =$

459    $0.0, \alpha = 1.0$) bands are shown in Figs. S5a and b, respectively. Here, we used the following sets

460   of the parameters for our analysis in this article: $F_{ana} = 55$, which corresponds to the time

461 window in the analysis of experimental data. $F_{wait} = 76$, with around which the band front can

462 propagate across one ROI. $F_{out} = 5$, which has been empirically determined. The duration

463 between each frame is $dt = 0.2$ in the unit of time of our numerical simulation.

464   Secondly, using these near-front ROIs, we calculate the histograms of migration direction

465 $(d\mathbf{r}_i(t)/dt)/|d\mathbf{r}_i(t)/dt|$ for each ROI using all the F_{ana} frames (t) and the particles (i) in it at

466 each frame. Then, we plot only the histograms for the ROIs which have the top eight and nine

467 peak probability densities for CFL-induced and alignment-induced bands, respectively. The

468 results are plotted in Figs. S5c and d, respectively. One can find the clear difference in these

469 histograms between the CFL-induced and alignment-induced bands. The peak position and

470 height for the CFL-induced band have large varieties, whereas those for alignment-induced

471 band are less distributed. Furthermore, the peaks for the CFL-induced band are much higher

472 than those for alignment-induced band. Figure 3i of the main text and Fig. S5e plot three typical

473 histograms from Fig. S5c and d, respectively.

474

481

482 **Competing interests** The authors declare that no competing interests exist.

483

484 **Author contributions**

485 M.H. and T.S. designed the research. M.H. and Y.W. performed the experiments, M.H.

486 and T.S. analyzed the data, H.K. provided KI cell and TgrB1⁻ KI cell and supervised the

487 experiments, T.H. developed and performed the numerical simulation, and M.H., T. H.,

488 H. K. and T. S. participated in writing the manuscript.

489

490 **Data availability**

491 The data that support the findings of this study are available from the corresponding

492 author upon reasonable request.

493

494

495 **Figure Legends**

496 **Figure 1**

497 **Segregation of cell density and formation of bands in non-chemotactic *D.***
498 ***discoideum* KI cell. a,** The density profile of three time points with a time interval of 15
499 min indicated by color-coding (red t=0, green 15min, blue 30min). Brighter color
500 indicates higher density. Five (left) and 25 (right) hours after incubation. See also
501 Supplementary Movie 1. **b,** The intensity profile along the line indicated in (a), showing
502 a periodic distribution of high-density regions. The inset shows a power spectrum of the
503 intensity profile, indicating that the spatial interval was about 1 mm. **c,** Time evolution
504 of phase-contrast image of high-density region (dotted lines) at t=2110, 3150, 4200 sec.,
505 respectively. The time points correspond to that in Supplemental Movie 2. **d,** High
506 magnification images of low-density region (i) and high-density region (ii). Arrows
507 indicate the migration directions of cells.

508

509 **Figure 2**

510 **Analysis of single cell migrations inside and outside the band. a,** Trajectories of
511 single cells inside (red) and outside (black) the band. These trajectories were taken from
512 the data shown in Fig. 1c. **b,c,** The distributions of the migration speed (b) and
513 migration direction (c) inside (pink) and outside (blue) the band. **d,** Mean squared
514 displacement (MSD) of cell motions inside the band (red), before entering the band
515 (green) and after leaving the band (blue) **e,** Scatter plot of the band speed v_w against the
516 cell speed $\langle v_{in} \rangle$ within the band. The number of bands investigated is $N = 10$.

517

518 **Figure 3**

519 **Analysis of heterogeneity within the ordered phase. a,** Spatial profile of the local
520 polar order parameter (solid lines) and the number of beads in the intervals (dotted
521 lines) in Fig. 1c. **b,** Scatter plot of band width against polar order parameter within the
522 band region. The number of bands studied is $N = 10$. **c,** Optical flow images in the
523 front region of a band t=405 (top) and within the band t=1083 (bottom). See also
524 Supplementary movies 3 **e,** Kymograph of the optical flow image along the line PQ
525 shown in c (top). The arrows indicate the average velocity of band $\langle v_b \rangle$ and the average
526 cell speed $\langle v_{in} \rangle$. **e,** Size-dependent squared local order parameter plotted against the
527 area S for the data shown in **c**. **f,** Probability distribution function (pdf) of the migration
528 direction within the band region obtained by the optical flow analysis shown in c. The
529 pdfs (i)-(iv) are obtained in the regions (i)-(iv) in c (bottom), respectively. Average pdf
530 is shown by the black line. **g,** Snapshot of simulation result showing a polar ordered

531 phase as a propagating band in the background of disordered phase. The color code

532 indicates the migration direction of individual particle as shown in **c**. See also

533 Supplementary movies 8. **h,** Magnification of squared area shown in **g**. The size of area

534 (20x20) is comparable to the whole area shown in **c**. Each arrow indicates the direction

535 of polarity. **i,** Probability distribution function of the migration direction within the band

536 region in the simulation (red, green and blue lines). For the choice of ROI, see

537 Supplementary text. Average pdf is shown by the black line.

538

539 **Figure 4**

540 **Contact following locomotion responsible for band propagation. a,** Snapshot of the

541 contact following locomotion. See also Supplementary movies 4. **b,** Representative time

542 evolution of collision of two cells. Colored arrows represent the same cell. See also

543 Supplementary movies 5. **c,** Histogram of the duration of two cell contacts for KI cell

544 (control). **d,** Schematic of angle a_1 (a_2), which is the angle of the velocity vector $\boldsymbol{v}_1$

545 ($\boldsymbol{v}_2$) with respect to the vector $\boldsymbol{d}$ connecting two cell centers. Then, the angle a is

546 obtained as the angular average of a_1 and a_2 , i.e., $A\cos a =$

547 $(\cos a_1 + \cos a_2)/2$, $A\sin a = (\sin a_1 + \sin a_2)/2$. **e,** Histogram of the angle a for the

548 KI cells that contact each other for >300 sec. **f.** Histogram of the duration of two cell

549 contacts for the *tgrb1* null mutant.

550

551

References

Ballerini M, Cabibbo N, Candelier R, Cavagna A, Cisbani E, Giardina I, Lecomte V, Orlandi A, Parisi G, Procaccini A, Viale M, Zdravkovic V. 2008. Interaction ruling animal collective behavior depends on topological rather than metric distance: Evidence from a field study. *Proc Natl Acad Sci USA* **105**:1232–1237. doi:10.1073/pnas.0711437105

Butt T, Mufti T, Humayun A, Rosenthal PB, Khan S, Khan S, Molloy JE. 2010. Myosin Motors Drive Long Range Alignment of Actin Filaments. *J Biol Chem* **285**:4964–4974. doi:10.1074/jbc.M109.044792

Chaté H, Ginelli F, Grégoire G, Raynaud F. 2008. Collective motion of self-propelled particles interacting without cohesion. *Phys Rev E* **77**:046113. doi:10.1103/PhysRevE.77.046113

Dormann D, Parent CA. 2002. Visualizing PI3 kinase-mediated cell-cell signaling during Dictyostelium development. *Curr Biol* **12**:1178–1188.

Fujimori T, Nakajima A, Shimada N, Sawai S. 2019. Tissue self-organization based on collective cell migration by contact activation of locomotion and chemotaxis. *Proc Natl Acad Sci USA* **116**:4291–4296. doi:10.1073/pnas.1815063116

Ginelli F, Peruani F, Bär M, Chaté H. 2010. Large-Scale Collective Properties of Self-Propelled Rods. *Phys Rev Lett* **104**:184502. doi:10.1103/PhysRevLett.104.184502

Haeger A, Wolf K, Zegers MM, Friedl P. 2015. Collective cell migration: guidance principles and hierarchies. *Trends in Cell Biology* **25**:556–566. doi:10.1016/j.tcb.2015.06.003

Hashimura H, Morimoto YV, Yasui M, Ueda M. 2019. Collective cell migration of Dictyostelium without cAMP oscillations at multicellular stages. *Commun Biol* **2**:34. doi:10.1038/s42003-018-0273-6

Hiraiwa T. 2019. Two types of exclusion interactions for self-propelled objects and collective motion induced by their combination. *Phys Rev E* **99**:012614. doi:10.1103/PhysRevE.99.012614

Hiraiwa T, Nagamatsu A, Akuzawa N, Nishikawa M, Shibata T. 2014. Relevance of intracellular polarity to accuracy of eukaryotic chemotaxis. *Phys Biol* **11**:056002. doi:10.1088/1478-3975/11/5/056002

Hirose S, Benabentos R, Ho H-I, Kuspa A, Shaulsky G. 2011. Self-recognition in social amoebae is mediated by allelic pairs of tiger genes. *Science* **333**:467–470. doi:10.1126/science.1203903

Hirose S, Santhanam B, Katoh-Kurosawa M, Shaulsky G, Kuspa A. 2015.

588   Allorecognition, via TgrB1 and TgrC1, mediates the transition from unicellularity

589   to multicellularity in the social amoeba Dictyostelium discoideum. *Development*

590   **142**:3561–3570. doi:10.1242/dev.123281

591   Kida Y, Pan K, Kuwayama H. 2019. Some chemotactic mutants can be progress

592   through development in chimeric populations. *Differentiation* **105**:71–79.

593   doi:10.1016/j.diff.2019.02.001

594   Kuwayama H. 2013. Biological soliton in multicellular movement. *Sci Rep* **3**:2272.

595   doi:10.1038/srep02272

596   Kuwayama H, Ishida S, Van Haastert PJ. 1993. Non-chemotactic Dictyostelium

597   discoideum mutants with altered cGMP signal transduction. *J Cell Biol* **123**:1453–

598   1462. doi:10.1083/jcb.123.6.1453

599   Kuwayama H, Obara S, Morio T, Katoh M, Urushihara H, Tanaka Y. 2002. PCR-

600   mediated generation of a gene disruption construct without the use of DNA ligase

601   and plasmid vectors. *Nucleic Acids Res* **30**:E2–2. doi:10.1093/nar/30.2.e2

602   Li B, Sun SX. 2014. Coherent motions in confluent cell monolayer sheets. *Biophys J*

603   **107**:1532–1541. doi:10.1016/j.bpj.2014.08.006

604   Li C-LF, Chen G, Webb AN, Shaulsky G. 2015. Altered N-glycosylation modulates

605   TgrB1- and TgrC1-mediated development but not allorecognition in Dictyostelium.

606   *J Cell Sci* **128**:3990–3996. doi:10.1242/jcs.172882

607   Li D, Wang Y-L. 2018. Coordination of cell migration mediated by site-dependent cell–

608   cell contact. *Proc Natl Acad Sci USA* **115**:10678–10683.

609   doi:10.1073/pnas.1807543115

610   Marchetti MC, Joanny J-F, Ramaswamy S, Liverpool TB, Prost J, Rao M, Simha RA.

611   2013. Hydrodynamics of soft active matter. *Rev Mod Phys* **85**:1143–1189.

612   doi:10.1103/RevModPhys.85.1143

613   Ohta T, Yamanaka S. 2014. Soliton-like behavior of traveling bands in self-propelled

614   soft particles. *Progress of Theoretical and Experimental Physics* **2014**:11J01–0.

615   doi:10.1093/ptep/ptt111

616   Solon AP, Chaté H, Tailleur J. 2015. From Phase to Microphase Separation in Flocking

617   Models: The Essential Role of Nonequilibrium Fluctuations. *Phys Rev Lett*

618   **114**:068101. doi:10.1103/PhysRevLett.114.068101

619   Sumino Y, Nagai KH, Yoshikawa K, Chaté H, Oiwa K. 2012. Large-scale vortex lattice

620   emerging from collectively moving microtubules. *Nature* **483**:448–452.

621   doi:10.1038/nature10874

622   Suzuki R, Weber CA, Frey E, Bausch AR. 2015. Polar pattern formation in driven

623   filament systems requires non-binary particle collisions. *Nat Phys* **11**:839–843.

624   doi:10.1038/nphys3423

625   Szabó B, Szöllösi GJ, Gönci B, Jurányi Z, Selmeczi D, Vicsek T. 2006. Phase transition

626   in the collective migration of tissue cells: Experiment and model. *Phys Rev E*

627   **74**:061908. doi:10.1103/PhysRevE.74.061908

628   Takeuchi R, Tamura T, Nakayashiki T, Tanaka Y, Muto A, Wanner BL, Mori H. 2014.

629   Colony-live--a high-throughput method for measuring microbial colony growth

630   kinetics--reveals diverse growth effects of gene knockouts in Escherichia coli. *BMC*

631   *Microbiol* **14**:171. doi:10.1186/1471-2180-14-171

632   Vicsek T, Czirók A, Ben-Jacob E, Cohen I, Shochet O. 1995. Novel Type of Phase

633   Transition in a System of Self-Driven Particles. *Phys Rev Lett* **75**:1226–1229.

634   doi:10.1103/PhysRevLett.75.1226

635   Vicsek T, Zafeiris A. 2012. Collective motion. *Physics Reports* **517**:71–140.

636   doi:10.1016/j.physrep.2012.03.004

637   Weber CA, Semmrich C. 2010. Polar patterns of driven filaments. *Nature* **467**:73–77.

638   doi:10.1038/nature09312

639   Williams JG. 2010. Dictyostelium finds new roles to model. *Genetics* **185**:717–726.

640   doi:10.1534/genetics.110.119297

641   Wioland H, Woodhouse FG, Kessler JO, Goldstein RE. 2013. Confinement stabilizes a

642   bacterial suspension into a spiral vortex. *Phys Rev Lett* **110**:268102.

643   doi:10.1103/PhysRevLett.110.268102

644   Zhang HP, Be'er A, Florin E-L, Swinney HL. 2010. Collective motion and density

645   fluctuations in bacterial colonies. *Proc Natl Acad Sci USA* **107**:13626–13630.
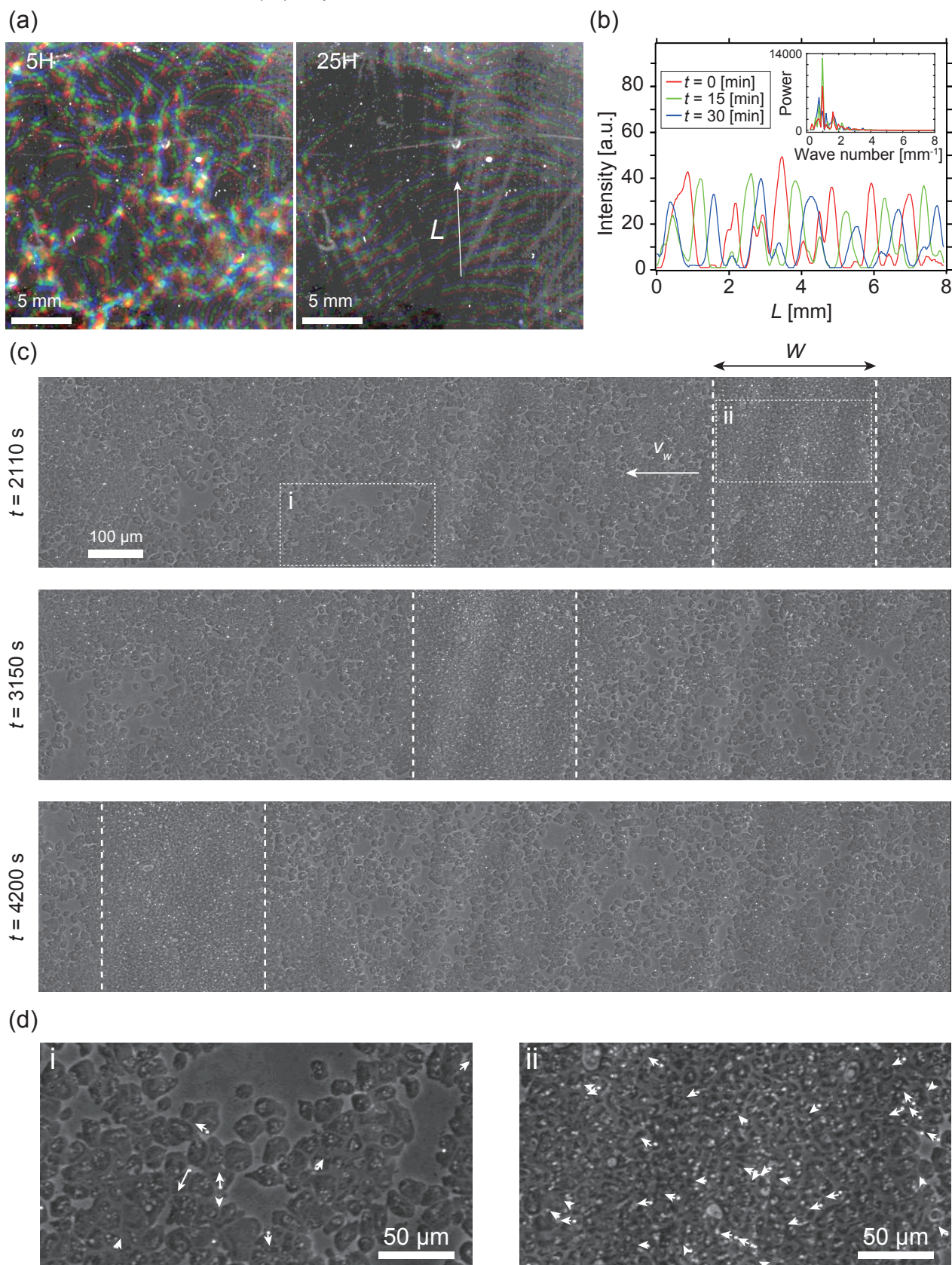
646   doi:10.1073/pnas.1001651107
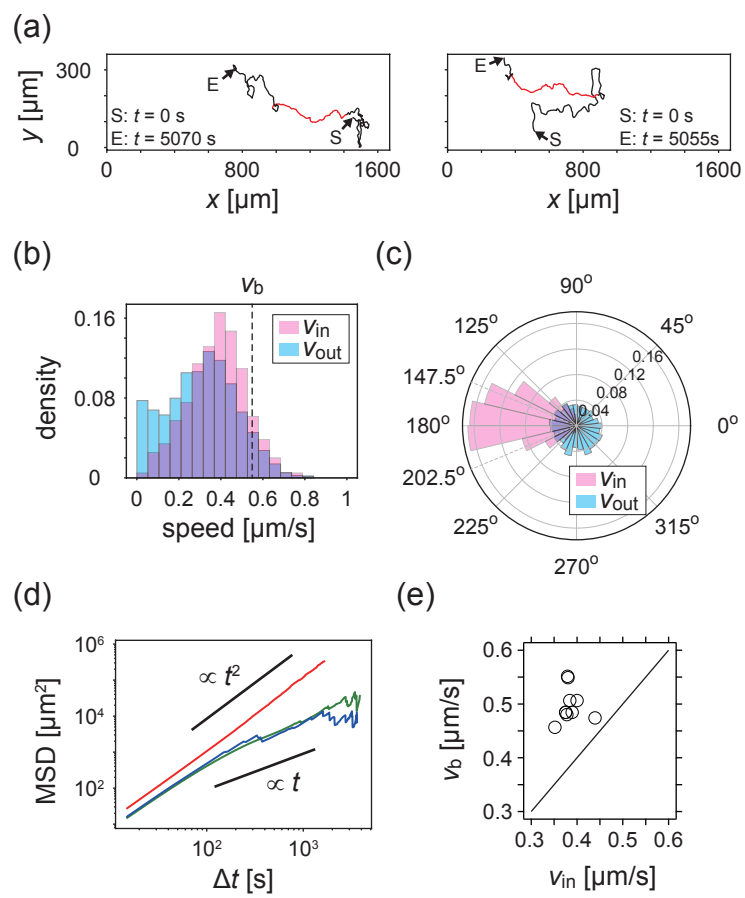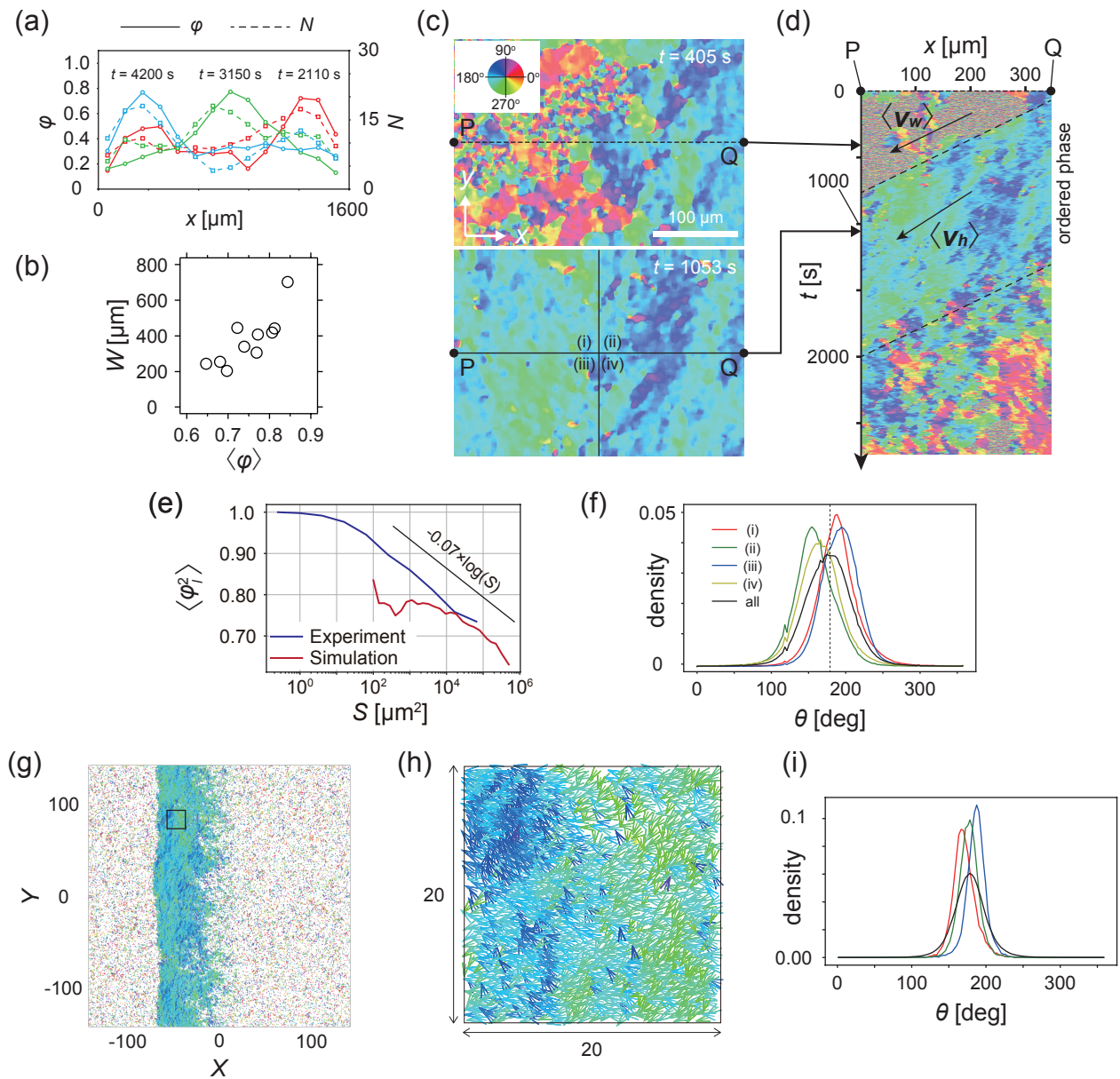
647

Fig.1

Fig.2
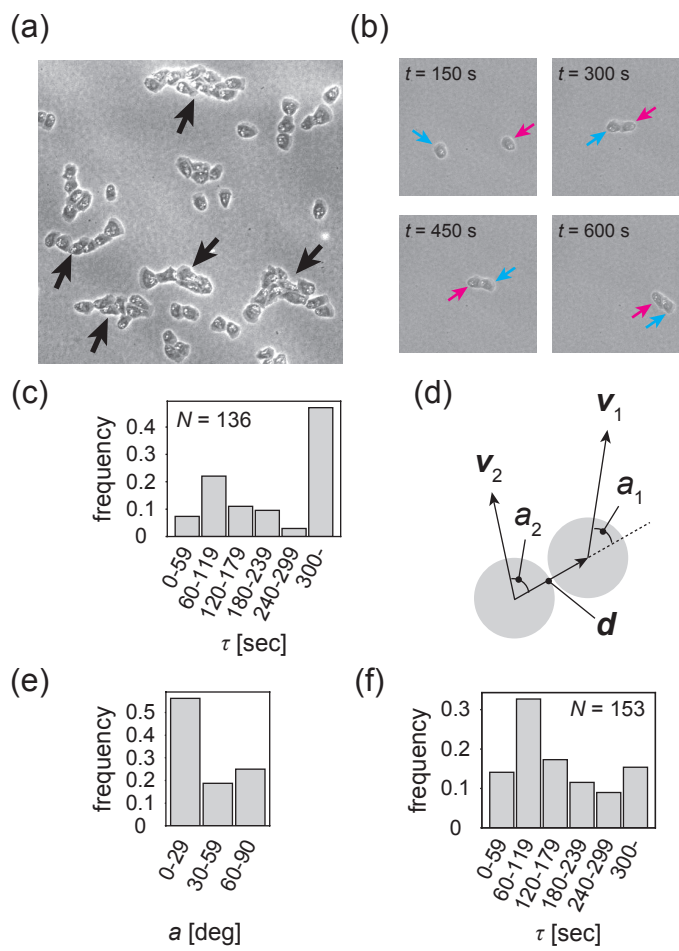
(a)

(b)

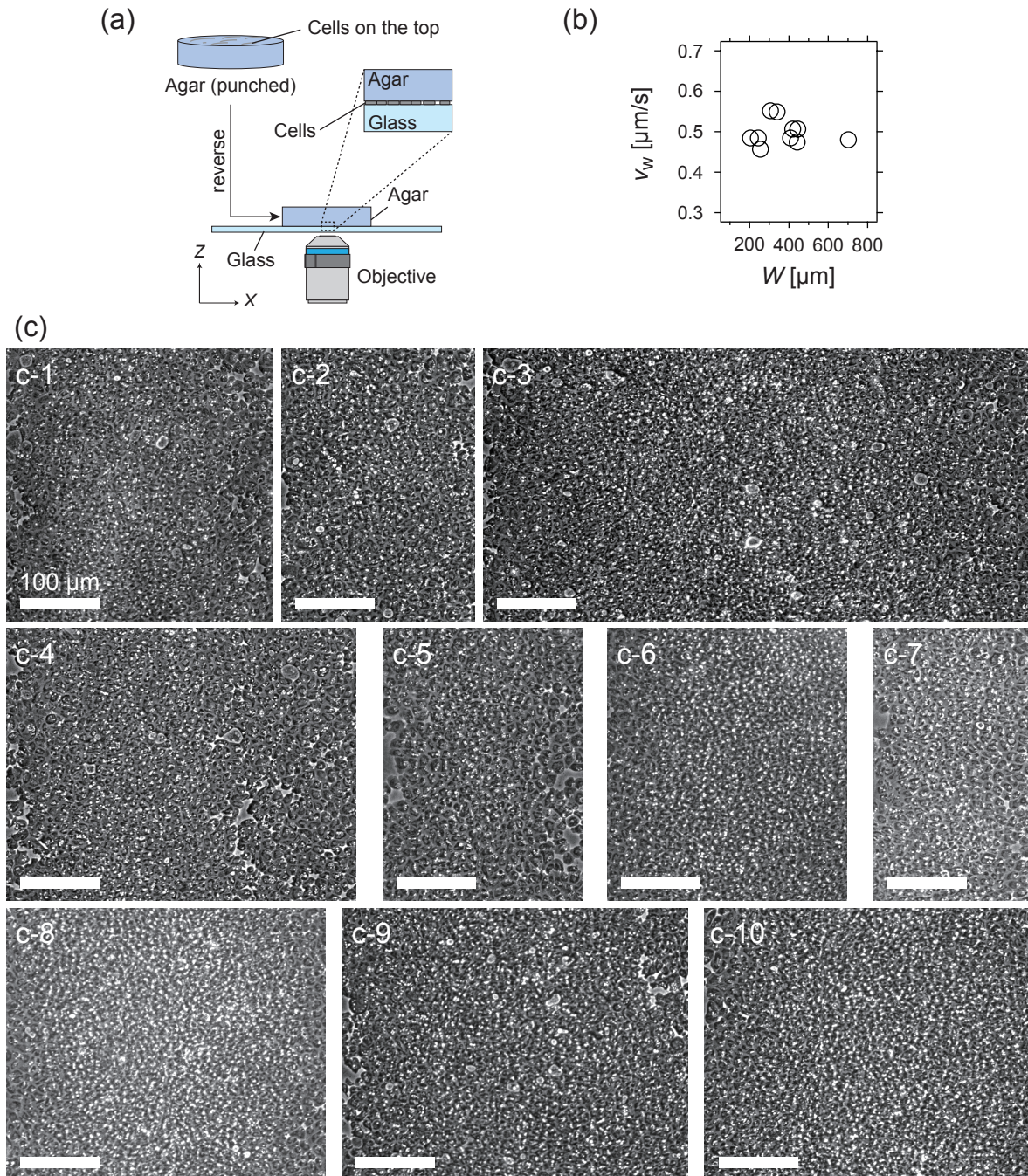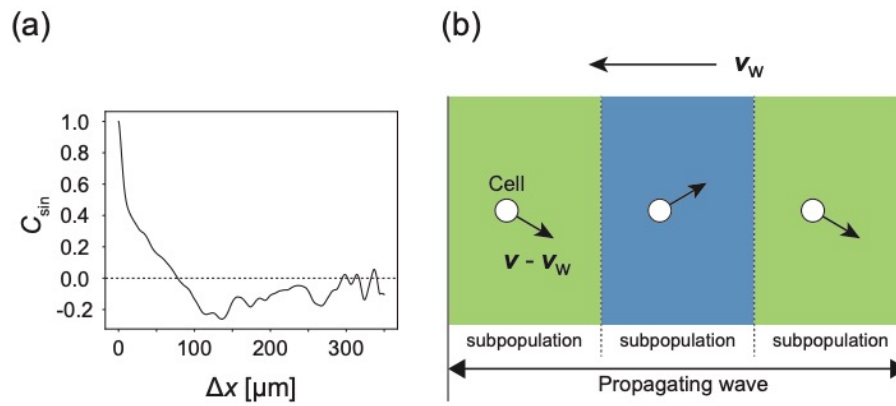(c)

(d)

(e)

Fig.3

Fig.4

(a)

(b)

(c)

(d)

(e)

(f)

Supplementary Figure 1 | (a) Experimental setup for the microscopic observation of the polar pattern formation. (b) Relationship between the propagation speed v_w and size of the wave W. (c) Snapshots of propagating band. The number of waves studied is N =10. (c-1) $W = 340$ μm; (c-2) $W = 244$ μm; (c-3) $W = 702$ μm; (c-4) $W = 445$ μm; (c-5) $W = 255$ μm; (c-6) $W = 306$ μm; (c-7) $W = 204$ μm; (c-8) $W = 408$ μm; (c-9) $W = 442$ μm; (c-10) $W = 419$ μm.

Supplementary Figure 2 | (a) **Autocorrelation function of transverse motion with respect to the wave propagation direction** $C_{\sin}(\Delta x)$, indicating that the typical width of the stripe was around 125 μm. (b) Illustration of the cell migration within the formed stripes in the co-moving frame. Arrows from cells indicate the direction of motion relative to the velocity vector of wave propagation.
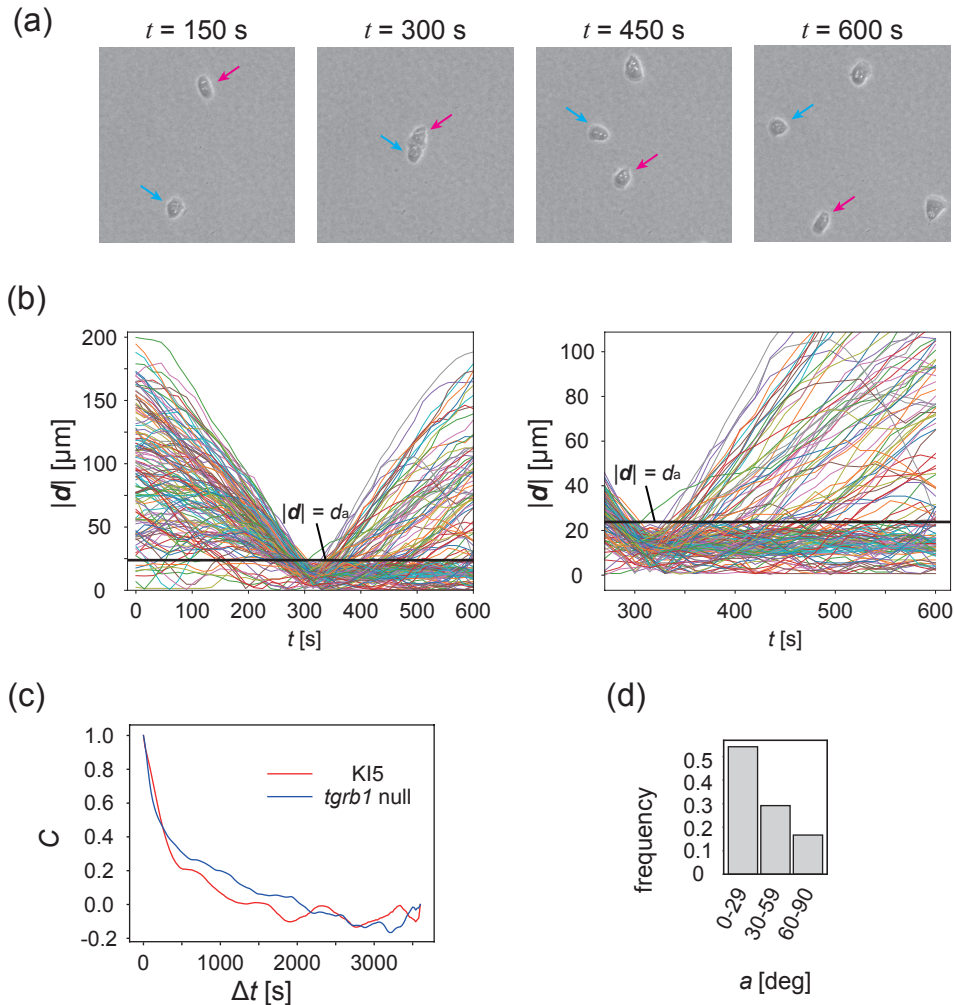
Supplementary Figure 3 | (a) Another example of time evolution of collision of two cells. (b) Time series of distance between two cells $|d|$. Each line is a data obtained from different cell pairs. Black horizontal line means $|d| = d_a$. Time series of $|d|$ after the collision ($t = 300$) is magnified in the right panel. (c) The velocity auto-correlation functions $C(\tau)$ of the isolated cells. Red line: KI cell. Blue line: *tgrb1* null mutant. (d) Histogram of the CFL angle a for the *tgrb1* null mutant cells that contact each other for >300 sec.
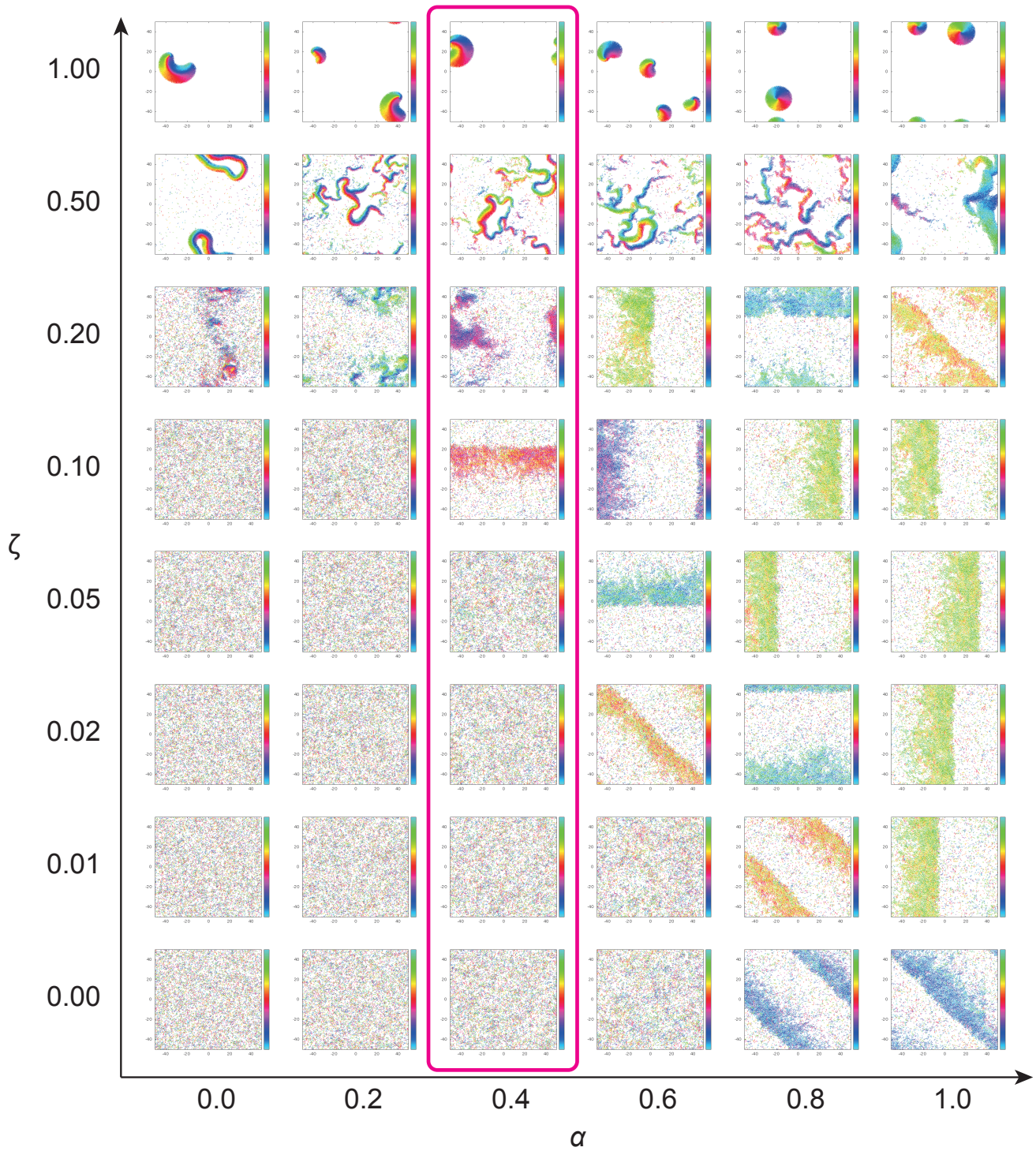
Supplementary Figure 4 | Phase diagram of the agent-based simulation for changes of CFL α and the alignment effect ζ. A region where $\alpha = 0.4$ is surrounded by the pink line.
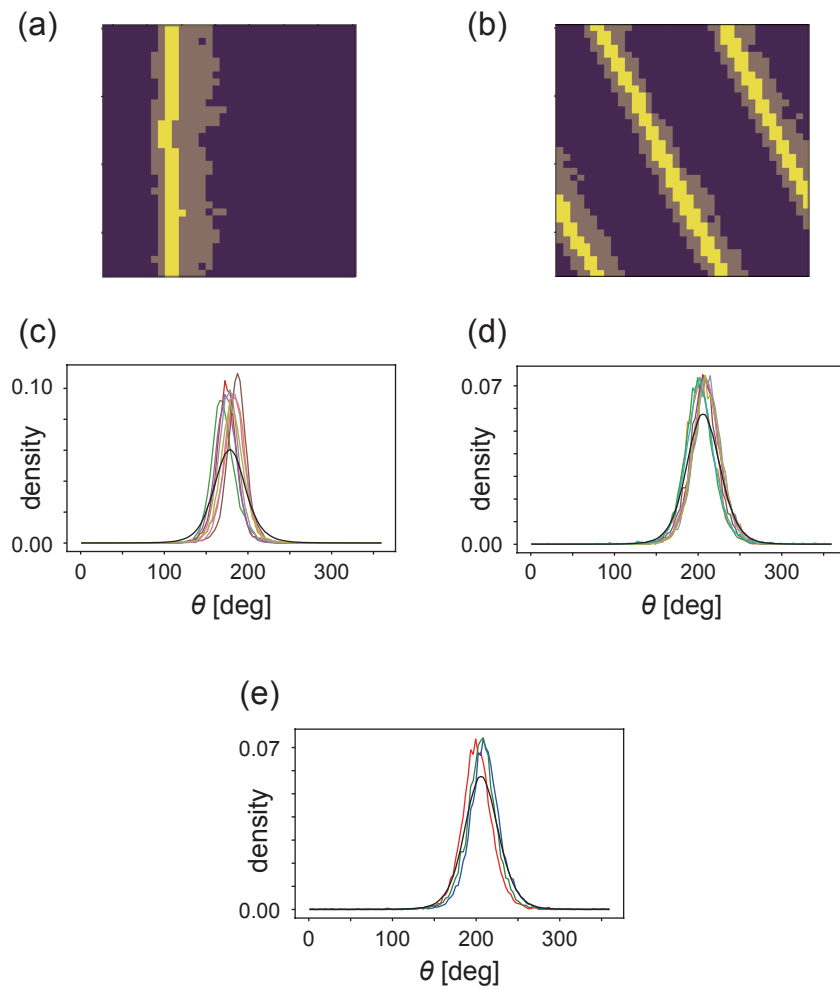
Supplementary Figure 5 | (a, b) The regions of interest used in the analyses (bright yellow) within the wave (dark yellow) for (a) CFL-induced and (b) alignment-induced waves, respectively. Analysis method to pick up these ROIs is found in Methods. (c, d) Pdfs of the migration direction within the wave region with the top eight and nine peak probability densities for (c) CFL-induced and (d) alignment-induced waves, respectively. (e) Typical pdfs for alignment-induced waves extracted from (d).

Supplementary Movie 1 | Macroscopic observation of the propagating bands.

The movie was taken every 15 min for 28.5 hours. Video acceleration: 11400 × real time.

Supplementary Movie 2 | Microscopic observation of the propagating bands.

The movie was taken every 15 s for 1.66 hours. Video acceleration: 230 × real time.

Supplementary Movie 3 | Propagating band with overlaying the coloring based on the optical flow analysis.

The movie was taken every 3 s for 39.5 min. Video acceleration: 151 × real time.

Supplementary Movie 4 | Migration of the KI cells in the low-density region.

The movie was taken every 15 s for 2 hours. Video acceleration: 378 × real time.

Supplementary Movie 5 | A binary collision of the KI cells in the low-density assay.

The movie was cropped from the movie of the low-density assay with a length of 10.25 min. Video acceleration: 153 × real time.

Supplementary Movie 6 | Macroscopic observation of the population of *tgrb1* null mutant.

The movie was taken every 15 min for 28.5 hours. Video acceleration: 11400 × real time.

Supplementary Movie 7 | Microscopic observation of the population of *tgrb1* null mutant.

The movie was taken every 15 s for 1.25 hours. Video acceleration: 225× real time.

Supplementary Movie 8 | Propagating band formation generated in the agent-based simulation.

The color code indicates the migration direction of individual particle as shown in Fig 3**c**. Arrows indicate the direction of polarity.